JOURNAL OF GEOPHYSICAL RESEARCH, VOL. 115, B05303, doi:10.1029/2009JB006582, 2010

Observations of *S*410*p* and *S*350*p* phases at seismograph stations in California

Lev Vinnik,[1] Yong Ren,[2,3] Eleonore Stutzmann,[2] Veronique Farra,[2] and Sergey Kiselev[1]

Received 30 April 2009; revised 4 November 2009; accepted 2 December 2009; published 5 May 2010.

[1] We analyze a new set of seismic data from seismograph stations in California. This data set consists of nearly 5000 *S* receiver functions for 47 seismograph stations. As a rule, the stacked SRFs display a distinct *S*410*p* seismic phase (*S* wave converted to *P* at the 410 km discontinuity). The wave paths of *S*410*p* sample the upper mantle beneath California and the neighboring region of the Pacific. In northernmost California the *S*410*p* travel times are close to those of the IASP91 global model. Further south, *S*410*p* usually arrives about 2 s earlier than predicted by the IASP91 model. This early arrival can be explained either by an anomalously high *Vp*/*Vs* velocity ratio (1.9 in a 125 km thick layer of the upper mantle versus 1.8 in IASP91), by a depression of the 410 km discontinuity of 15 km, or by a combination of both effects with smaller amplitudes. We observe systematically *S*350*p* phase which is converted from a negative discontinuity (with a lower *S* velocity at the lower side) near a depth of 350 km. The observations of *S*350*p* are indicative of a low *S* velocity layer a few tens of kilometers thick atop the 410 km discontinuity beneath southern California and the neighboring oceanic region. Some receiver functions also display *S*480*p* phase, which is interpreted as evidence of an intermittent low-velocity layer in the transition zone.

Citation: Vinnik, L., Y. Ren, E. Stutzmann, V. Farra, and S. Kiselev (2010), Observations of *S*410*p* and *S*350*p* phases at seismograph stations in California, *J. Geophys. Res.*, *115*, B05303, doi:10.1029/2009JB006582.

1. Introduction

[2] The geologic history of western North America over the past 150 million years has been shaped by eastward subduction of oceanic tectonic plates [*Atwater*, 1989]. The major tectonic feature of California, the San Andreas fault, is the boundary between the Pacific and North American plates that evolved from a subduction boundary between the Farallon and the North American plates to the present transform fault. The San Andreas fault ends near the latitude of 40°N at the Mendocino triple junction where the North America, Pacific, and Gorda plates meet (Figure 1). Subduction of a remnant of the Farallon plate, the Juan de Fuca plate, continues north of 40°N.

[3] The upper mantle beneath California has been a focus of numerous seismic studies with techniques which include body wave travel-time tomography [e.g., *Benz et al.*, 1992; *Thurber et al.*, 2009], surface waves [e.g., *Tanimoto and Sheldrake*, 2002; *Yang and Forsyth*, 2006; *Yang et al.*, 2008], and receiver functions [e. g., *Gurrola and Minster*, 1998; *Chevrot et al.*, 1999; *Vinnik et al.*, 1999; *Simmons and Gurrola*, 2000; *Ramesh et al.*, 2002; *Zandt et al.*, 2004]. The San Andreas fault separates regions with differing upper mantle velocities: the North American side is systematically slow relative to the Pacific side [*Tanimoto and Sheldrake*, 2002]. The *SS* phases from southern earthquakes arrive at coastal stations like SBC, PKD, SAO, and BRIB (Figure 1) much earlier than at equidistant stations in eastern California [*Melbourne and Helmberger*, 2001]. This difference implies that the coastal paths sample the upper mantle with a thick high-velocity lid, which becomes thin to the east, in qualitative agreement with the work of *Tanimoto and Sheldrake* [2002]. Lateral velocity variations in the upper mantle beneath California reach 10% for *S* waves [*Yang and Forsyth*, 2006] and are correlated with tectonics. In particular, the bend of the San Andreas fault near 35°N is responsible for the origin of the Transverse Range, and various seismic data reveal relatively high velocities beneath this range which are interpreted in terms of a sinking high-velocity mantle lithosphere. Another region of comparable complexity is the southern Great Valley and the Sierra Nevada mountains [*Zandt et al.*, 2004].

[4] While the upper mantle at depths less than about 250 km is reasonably well sampled by previous studies, the structure at larger depths still is not known in sufficient detail. The discontinuities at depths of 400 ± 100 km on a regional scale are often investigated with *Ps* (*P* to *S*) converted phases in *P* receiver functions, but the recordings of these phases suffer from reverberations in the lithosphere

[1]Institute of Physics of the Earth, Moscow, Russia.
[2]Institut de Physique du Globe de Paris, Paris, France.
[3]School of Earth and Environment, University of Leeds, Leeds, UK.

0148-0227/10/2009JB006582

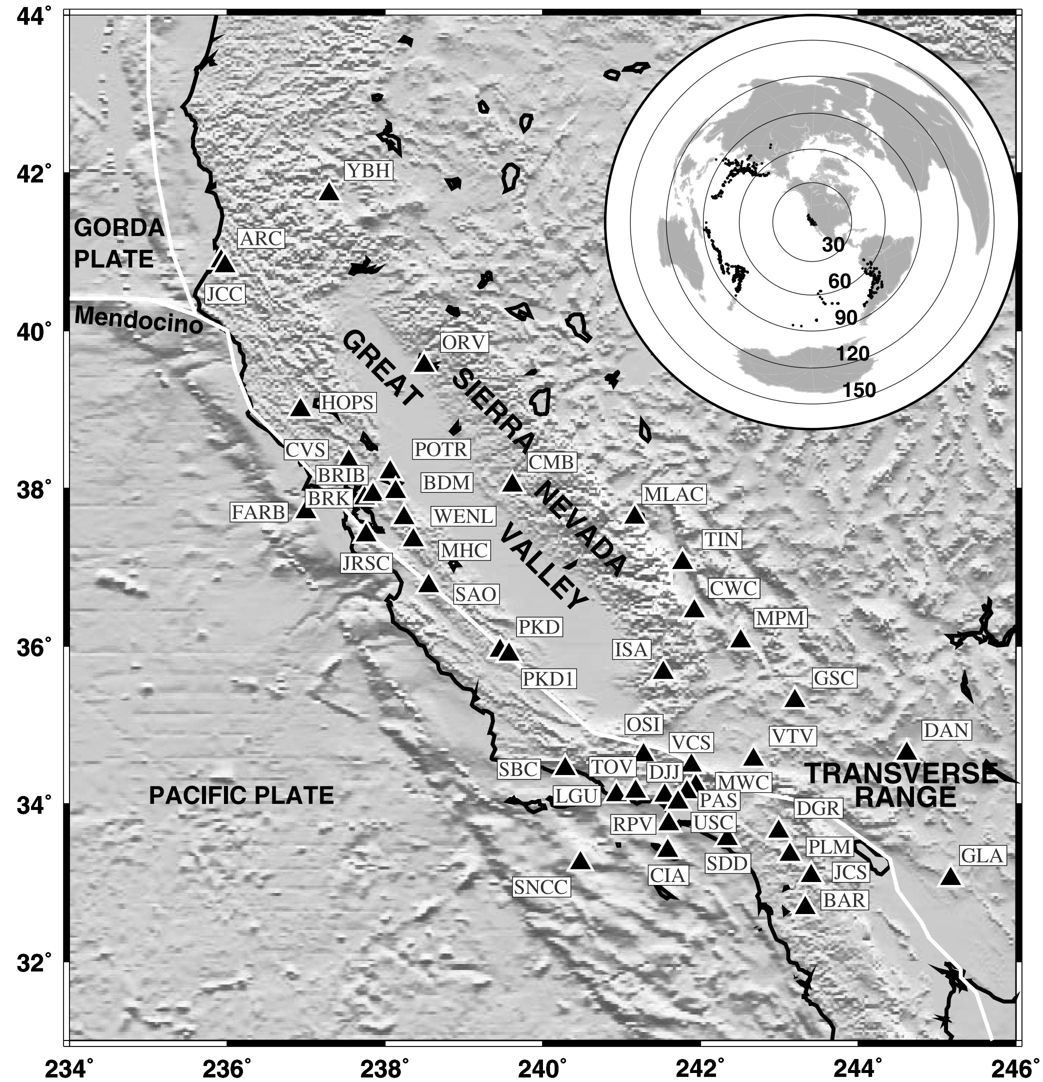

Figure 1. Map of the study region with seismograph stations (triangles) and locations of the earthquakes (inset).

and large anelastic attenuation of *S* waves. Here, instead of *Ps* phases in *P* receiver functions, we use *Sp* (*S* to *P*) converted phases in *S* receiver functions (SRFs) [*Farra and Vinnik*, 2000]. The advantage of the *S* receiver functions lies not only in the early arrivals of the *Sp* phases relative to lithospheric reverberations, but also in the different effect of anelastic attenuation. The largest anelastic attenuation is observed in the upper mantle at depths less than about 300 km. The *S*410*p* phase propagates at these depths as *P* wave, which is less attenuated than *S* wave. As the receiver function is the result of deconvolution by the parent wave (*P* and *SV* for the *P* and *S* receiver functions, respectively), the *S*410*p* phase is amplified with respect to the *P*410*s* phase from the same discontinuity. Under realistic assumptions on the quality factor *Q* in the upper mantle (Qs = 50, $Qp = 2.2Qs$), the amplification factor of *S*410*p* relative to *P*410*s* at a period of 10 s is close to 2. Finally, the piercing points of *S*410*p* are at a distance of several hundred kilometers from the station, and *S*410*p* samples the oceanic upper mantle by observations on land.

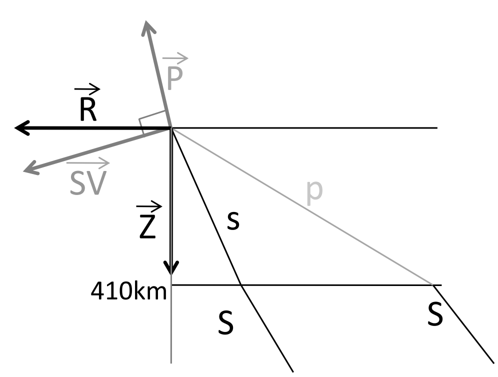

Figure 2. Sketch of the coordinate system.

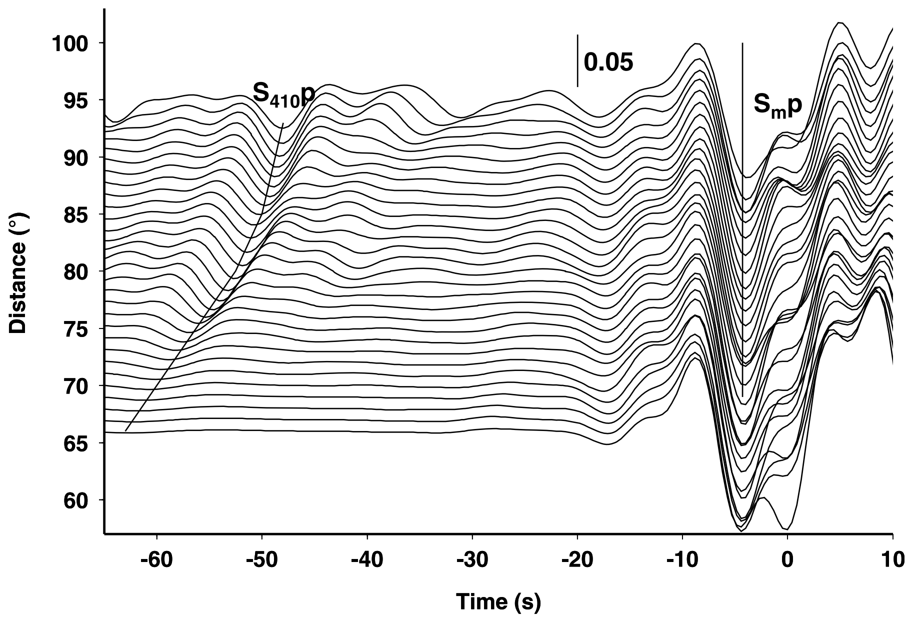

Figure 3. Synthetic *P* components of *S* receiver functions (SRFs) for the IASP91 Earth model. *Smp* and *S*410*p* are *S*-to-*P* converted phases from the Moho and the 410 km discontinuity, respectively.

[5] We address the following issues: depth of the 410 km discontinuity, fine *S* velocity structure in the vicinity of this discontinuity, and *Vp*/*Vs* ratio in the upper mantle.

2. Method

[6] Calculation of the SRF [*Farra and Vinnik*, 2000] involves seismogram decomposition into *SV*, *P*, *T*, and *M* components (Figure 2). The SV axis corresponds to the principal *S* wave particle motion direction in the wave propagation plane. The angle between the *SV* axis and the radial direction is determined from the covariance matrix of the vertical and radial components of the *S* wave. The *P* axis is normal to *SV* in the same plane. The *S* wave is not recorded on the *P* component, and this makes the *P* component optimal for detecting *Sp* phases. *T* is normal to the wave propagation plane, and *M* is the principal *S* particle motion component in the plane containing the *SV* and *T* components. The angle θ between the axes *SV* and *M* is controlled by the focal mechanism of the earthquake. The *P* component is deconvolved by the *M* component.

[7] In radially stratified isotropic Earth, the *Sp* converted phase is generated by the *SV* component of the incoming *S* wave. In case of azimuthal anisotropy or dipping interfaces, the *Sp* converted phase can also be generated by the *SH* component, but separation of these two effects requires observations in many azimuths, which is not the case in our data. In the *SV*-to-*P* converted phases the effect of the isotropic component of the medium is strongly dominant, and these phases present the basis of our study. To isolate the *Sp* phases generated by *SV* and optimize the signal-to-noise ratio, the individual *P* components of many events are stacked with weights depending on θ and the level of noise. The result of stacking is the *P* component deconvolved by the *SV* component of the *S* wave and normalized to the amplitude of the *SV* component. The procedure involves evaluation of σ, the root-mean-square (RMS) value of noise in the stack from noise in the individual receiver functions. The estimates of noise in the individual SRFs are usually obtained in the window from −60 to −20 s. This estimate of RMS is very consistent with that obtained by bootstrap resampling [*Vinnik and Farra*, 2007].

[8] To account for the difference in slowness between the *S* and *Sp* phases from deep discontinuities, the individual receiver functions should be stacked with appropriate moveout corrections. The accurate calculation of the correction requires the velocity model, the assumed depth of the discontinuity, and the slowness of *S*. For most upper mantle models *S*410*p* does not exist in the ray-theoretic limit at epicentral distances less than 79°. However, in actual seismic recordings and in the finite-frequency synthetics with a dominant period of several seconds, calculated with the reflectivity technique [*Fuchs and Mueller*, 1971], the signal of a smaller amplitude is observed at shorter distances (Figure 3), and part of our observations of the *S*410*p* phase is made at these distances (Table 1). To simplify the calculations of the moveout corrections, we use slant stacking of receiver functions, where the moveout correction is defined as the product of the trial slowness with respect to the *S* wave slowness (differential slowness) and the epicentral distance of the event with respect to the reference distance (differential distance). At the periods around 10 s and in the narrow range of the *S* wave slowness (between 12.3 s/° at a distance of 65° and 9.2 s/° at a distance of 90°), these moveout corrections are sufficiently accurate. The stack is calculated for the differential slownesses ranging from 0 to 1.2 s/°. In experiments with synthetics for global models like IASP91 [*Kennett and Engdahl*, 1991], the largest amplitude of *S*410*p* is obtained at a differential slowness around 0.5 s/°. A tilt of the converting interface or another form of lateral heterogeneity may change this value. Spe-

Table 1. List of the Data[a]

Stations	*Baz* (deg)	*D* (deg)	Ref *D* (deg)	Number of Recordings	*S*410*p* Time (s)	*S*410*p* Residual (s)	*S*350*p*	*S*450*p*
YBH	297.9	76.5	79	45	−55.4	−0.9		
YBH	241.2	83.3	84	80	−52.8	−1.5		+
YBH	134.3	81.5	84	35	−52.2	−0.8		
ARC+ JCC	302.0	70.2	76	97	−56.8	+0.1		
ARC+ JCC	237.7	81.3	83	108	−54.3	−2.5		
ORV	301.9	75.5	82	73	−52.0	+0.3		
ORV	239.2	83.1	81	140	−53.5	−0.6		
ORV	136.7	80.5	82	56	−52.1	+0.2	+	
HOPS	300.7	73.6	79	79	−55.6	−1.1	+	
HOPS	134.2	78.7	80	43	−57.0	−3.5	+	
BDM+ROTR+CVS	303.1	72.6	78	84	−56.7	−1.4		+
CMB	302.8	74.1	74	127	−58.8	−0.5		
CMB	237.4	83.2	83	175	−52.5	−0.7		
CMB	138.2	76.5	81	69	−54.9	−2.0	+	+
BRK+BRIB	301.8	73.9	77	107	−56.5	−0.4		+
BRK+BRIB	235.6	80.4	82	123	−54.6	−2.3		+
BRK+BRIB	135.4	78.6	80	83	−55.9	−2.4		
FARB	303.9	72.6	78	34	−55.0	+0.3		
FARB	231.8	77.6	79	34	−56.4	−1.9	+	
FARB	133.6	78.4	81	33	−55.0	−2.1		
MLAC+TIN+CWC	306.4	74.2	77	74	−56.4	−0.3		
MLAC+TIN+CWC	236.7	81.0	81	69	−53.9	−1.0	+	
MLAC+TIN+CWC	135.8	76.9	77	66	−57.0	−0.9	+	+
WENL	236.3	79.6	82	52	−53.5	−1.2	+	
WENL	140.0	77.8	81	35	−56.3	−3.4		
JRSC	303.8	72.7	77	77	−55.8	+0.3		+
JRSC	234.7	79.6	83	92	−54.5	−2.7		
JRSC	134.4	78.2	83	59	−54.5	−2.7		
MHC	302.9	74.2	76	104	−58.6	−1.7		
MHC	234.4	81.3	84	85	−54.2	−2.9		
MHC	135.5	77.3	81	68	−55.7	−2.8		
SAO	302.8	74.2	80	118	−54.3	−0.8		
SAO	235.1	80.0	82	153	−54.6	−2.3		
PKD+PKD1	303.9	76.5	80	67	−55.6	−2.1		+
PKD+PKD1	235.7	80.2	84	101	−54.4	−3.1		+
PKD+PKD1	137.6	76.7	79	62	−56.1	−1.6		
ISA+CWC+MPM	307.0	74.4	80	67	−55.1	−1.6		
ISA+CWC+MPM	236.9	80.2	83	99	−53.7	−1.9	+	
ISA+CWC+MPM	138.8	76.3	78	64	−57.2	−1.9	+	
MPM+GSC	307.3	75.1	82	71	−54.6	−2.3	+	+
MPM+GSC	237.1	80.4	80	82	−55.0	−1.5	+	+
MPM+GSC	140.1	75.6	79	65	−57.2	−2.7	+	
MWC+VCS+VTV	307.8	75.1	80	117	−54.5	−1.0	+	
MWC+VCS+VTV	237.4	80.2	82	83	−52.7	−0.4	+	
MWC+VCS+VTV	135.9	74.5	74	79	−58.7	−0.4	+	+
SBC+LGU+TOV+OSI	306.3	75.6	78	118	−57.0	−1.7	+	+
SBC+LGU+TOV+OSI	236.2	80.2	87	144	−51.4	−1.3	+	+
SBC+LGU+TOV+OSI	135.2	75.6	77	98	−58.5	−2.4	+	
PAS+DJJ+USC	306.6	75.9	80	91	−55.2	−1.7	+	+
PAS+DJJ+USC	236.2	80.1	84	112	−53.3	−2.0	+	
PAS+DJJ+USC	136.5	75.1	75	83	−59.3	−1.8	+	+
DGR+PLM	309.1	75.6	80	92	−56.5	−3.0	+	
DGR+PLM	236.1	80.0	82	77	−54.0	−1.7	+	
DGR+PLM	139.9	74.9	77	72	−58.6	−2.5	+	
SNCC+CIA+RPV+SDD	306.8	76.5	75	108	−58.4	−0.9	+	
SNCC+CIA+RPV+SDD	235.8	80.1	85	125	−53.6	−2.7	+	+
SNCC+CIA+RPV+SDD	135.1	74.6	75	94	−59.0	−1.5	+	+
DAN+GLA	310.8	75.3	78	85	−57.3	−2.0		+
DAN+GLA	239.0	81.2	82	68			+	+
DAN+GLA	144.3	74.5		62				+
BAR+JCS	310.6	75.1	80	73	−56.2	−2.7	+	
BAR+JCS	236.8	80.0	82	75	−53.8	−1.5	+	
BAR+JCS	136.6	72.7	75	44	−56.9	+0.6	+	+

[a]*Baz* is back azimuth. Columns labeled *D* and Ref *D* are for the average and reference epicentral distances, respectively. Amplitude ratios of *S*350*p*/*S*410*p* and *S*480*p*/*S*410*p* of at least 0.7 are marked by plus signs.

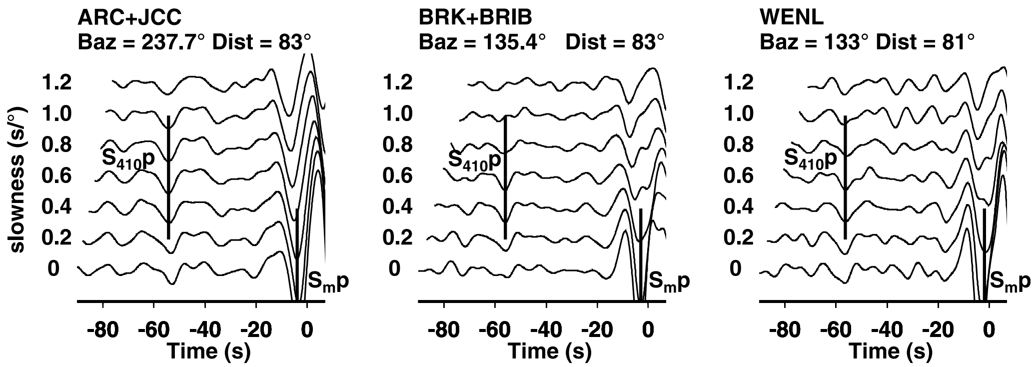

Figure 4. Examples of stacked *P* components of SRFs. The origin of the time axis corresponds to the arrival of *S*. Arrivals of *S*410*p* and *Smp* are marked by vertical lines.

cifically, a tilt of 2° changes the differential slowness by 0.1 s/°.

3. Observations and Analysis of *S*410*p*

[9] We have calculated more than 5000 *S* receiver functions from 46 stations in California (Table 1 and Figure 1). To optimize signal-to-noise ratio the records were low-pass-filtered with a corner frequency of 0.12 Hz. The individual receiver functions were stacked in a distance range from 65° to 90° in three back azimuth sectors: from 133° to 145°, from 231° to 239°, and from 297° to 311°. In each sector the receiver functions were stacked either for single stations or, if the number of recordings at a single station was small, for a few neighboring stations. The required number of the stacked receiver functions is in a range of several tens. Then the RMS value of noise is less than 0.01. The arrivals with the amplitudes of at least $\pm 3\sigma$ are regarded as signals. For the normal amplitude distribution this threshold makes false detections unlikely (probability of 0.3%). The *Sp* arrival time is measured relative to the *S* wave arrival; in other words, the *Sp* arrival time is the difference in time between the arrivals of *Sp* and *S*. For our sign convention, negative polarity of the *Sp* phase corresponds to a positive discontinuity (with a higher *S* velocity at the lower side of the discontinuity).

[10] Every stack contains the *Sp* phase from the Moho (*Smp*) with the largest amplitude at the 0 s/° differential slowness. *Smp* (Figure 4) is seen as a negative pulse at a time around −3 s. The positive swing at a time around −10 s is mainly a combined effect of the sidelobe of *Smp* and of the *Sp* phase from the boundary at a depth around 70 km between the high-velocity mantle lid and the underlying low *S* velocity zone. The *S*410*p* phase is detected with confidence in almost every stack and is seen at several traces; the largest amplitude of *S*410*p* as a rule is observed at a differential slowness between 0.2 and 1.0 s/°. Its largest amplitude in Figure 4 is at a differential slowness of 0.6 s/°, close to the theoretical value.

[11] In the distance range from 75° to 90°, the *SKS* seismic phase arrives within 30 s of *S* arrival time, and at around 83° they even arrive at the same time. There are three possible kinds of interaction between *S* and *SKS*: the contribution of *SKS* to the wave train is small relative to *S*, the contribution of *S* is small relative to *SKS*, and the contributions of *S* and *SKS* are comparable. In the first case the detected signal is *S*410*p*, and in the second case this is *SKS*410*p*. In the third case no signal is detected because the waveform used for deconvolution is strongly different from both *S* and *SKS*. *S*410*p* can be easily distinguished from *SKS*410*p* because it arrives about 10 s later than *SKS*410*p*. In our receiver functions the only detected signal is *S*410*p* with the implication that the *S* wave is dominant and the effect of interference between *S* and *SKS* is negligible.

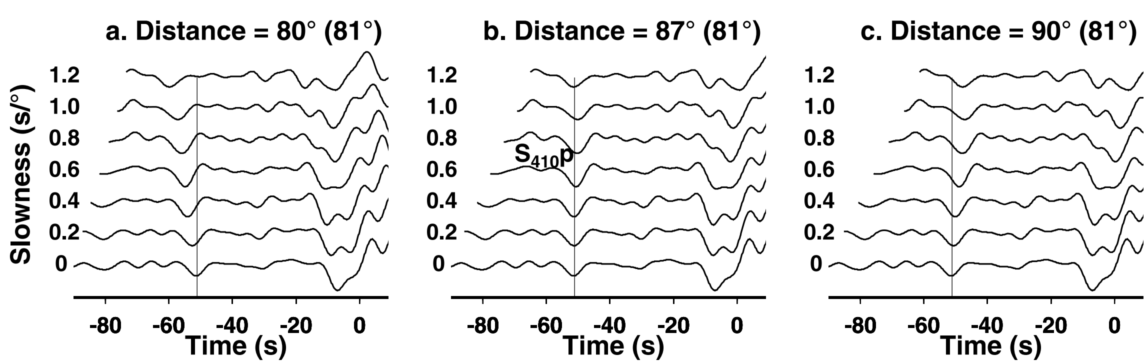

Figure 5. Examples of *S*410*p* arrival time for a reference epicentral distance of (a) 80°, (b) 87°, and (c) 90°. The average epicentral distance for the set of stacked receiver functions is 81°. The time is practically independent of slowness for the reference distance of 87°.

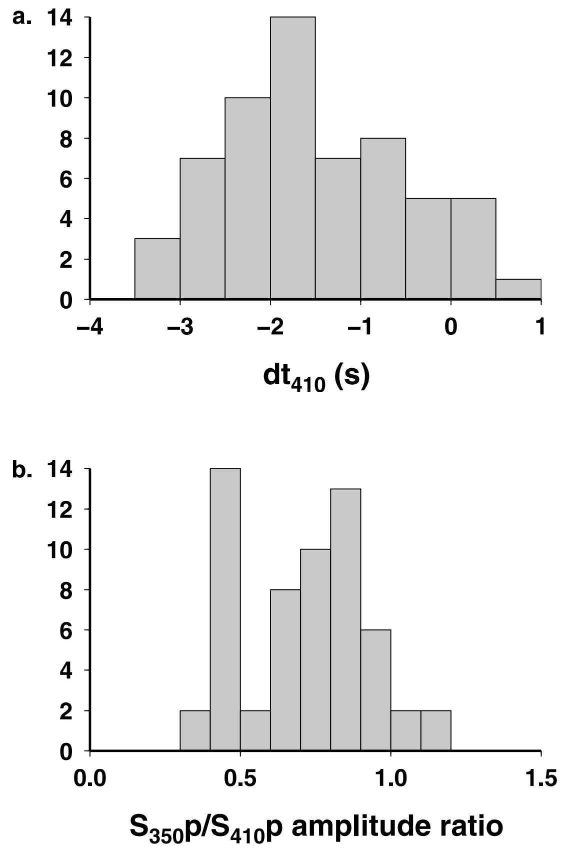

Figure 6. Histograms of (a) the arrival times of *S*410*p* and (b) of the amplitude ratio between the positive swing following *S*410*p* and *S*410*p*.

[12] Our first task is to measure the arrival time of the *S*410*p* phase with maximum accuracy. The detected signal is present in several traces of the stack, and the arrival time can differ between the traces by up to a few seconds (Figure 5). This effect may introduce an uncertainty in the measurement results, and it should be minimized. The dependence of the arrival time on differential slowness means that the average signal amplitude differs between the negative and positive differential distances. This dependence can be minimized by appropriate selection of the reference distance (the distance at which the moveout corrections change their sign). The optimum reference distance can be found by trial and error (Figure 5). It may differ by a few degrees from the average epicentral distance (Table 1). In Figure 5 the average distance is 81°, and the optimum reference distance is 87°. The optimum reference distance is larger because the amplitudes at the distances shorter than the critical distance of 79° are relatively small.

[13] A standard error of our measurements of the *S*410*p* arrival time thus performed is less than ±0.5 s. Most arrivals of *S*410*p* are early with respect to IASP91 model [*Kennett and Engdahl*, 1991], with residuals that reach −3.5 s (Table 1). The histogram of the residuals (Figure 6a) demonstrates that most residuals are between −0.5 and −3.0 s.

[14] We attribute the residual to the surface projection of the piercing point—the crossover of the raypath of *S*410*p* and the 410 km discontinuity. The shift of this projection relative to the seismograph station for several explored *P* and *S* velocity models changes from about 450 km at the epicentral distance of 90° to about 800 km at the epicentral distance of 79°. In the ray-theoretic limit *S*410*p* does not exist at epicentral distances shorter than 79°. Owing to the grazing incidence of the *P* wave at a depth of 410 km at the short distances, the location of the piercing point at these distances becomes highly uncertain, and *S*410*p* is formed in

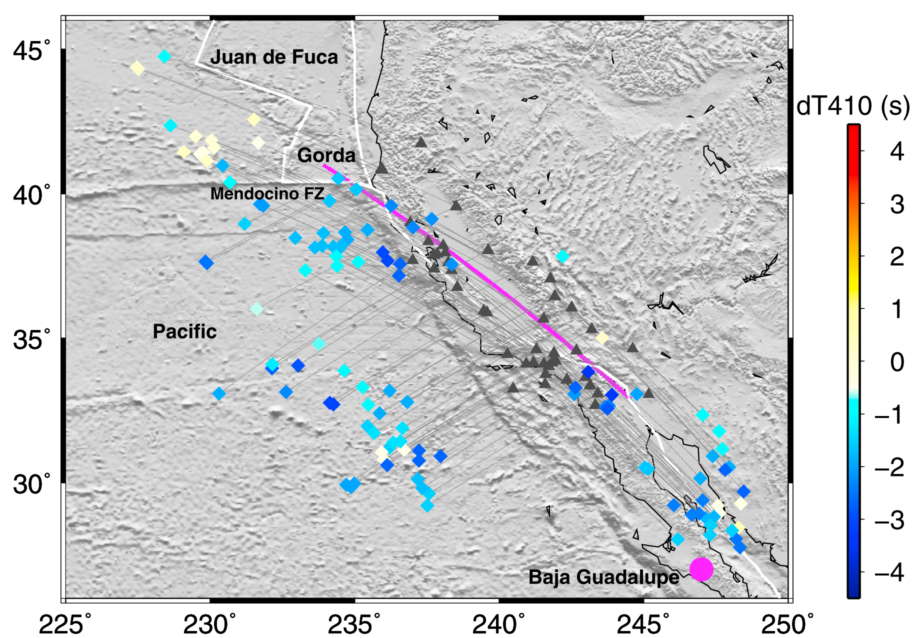

Figure 7. Surface projections of the piercing points of *S*410*p*. The related time residuals are shown by color code. Seismograph stations are shown by black triangles. The purple line is the vertical plane for common conversion point stacking. The purple circle is the center of the Baja Guadalupe hot spot.

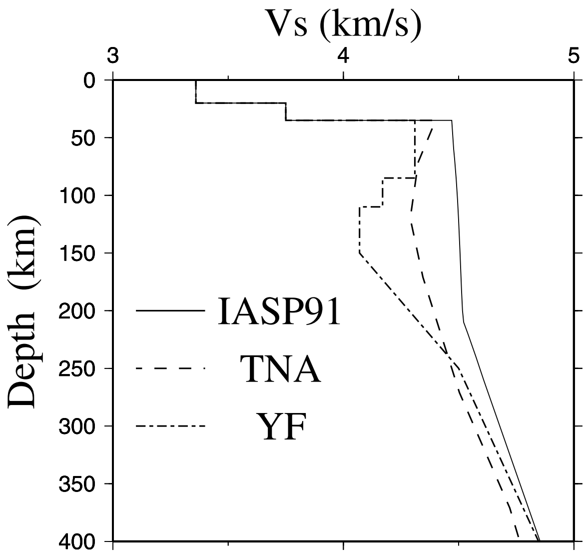

Figure 8. *S* velocity profiles for modeling the time residuals of *S*410*p*: IASP91 [*Kennett and Engdahl*, 1991], TNA [*Grand and Helmberger*, 1984], and YF [*Yang and Forsyth*, 2006].

a very large region. For the present purposes, at epicentral distances less than 79° we plot the piercing points at a distance of 800 km. In the map thus compiled (Figure 7) the large (around −2 s) negative residuals are dominant in both California and the neighboring region of the Pacific. A cluster of small negative and positive residuals is present in the Pacific to the north of the seismograph network.

[15] There are a few possible reasons for the negative residuals. They can be an effect of lateral heterogeneity. If, for example, the *S* wave propagates mostly in a low-velocity upper mantle, whereas the *P* wave leg of the *S*410*p* wave path is in the high-velocity mantle, the arrivals of *S*410*p* are early. Then the lateral heterogeneity would produce negative and positive residuals in the same area for the opposite directions of wave propagation. This, however, is not observed for the nearly opposite back azimuths of around 305° and 140° (Figure 7). Moreover, lateral heterogeneity along the wave path may affect the differential slowness of the *Sp* phase. However, observations of a differential slowness of *S*410*p* that deviate significantly from the standard 0.5 s/° are practically absent in our data.

[16] The residuals can be explained by differences between the actual velocity profiles and IASP91 model. We tested two *S* velocity models: TNA [*Grand and Helmberger*, 1984] and YF [*Yang and Forsyth*, 2006] (Figure 8), proposed for western North America and southern California, respectively. Both models display lower *S* velocities in the upper mantle than IASP91 and do not specify *P* velocities. In order to calculate the *S*410*p* arrival times we derived the corresponding *P* wave velocities by adopting the *Vp*/*Vs* velocity ratio of IASP91. Although the teleseismic *S* wave arrivals are delayed in TNA by several seconds relative to IASP91, the effect on the arrival time of *S*410*p* at a distance of around 80° is on the order of a fraction of a second (Figure 9). *S* velocities in the YF model are much lower than in TNA, but the absolute values of the residuals of *S*410*p* still are too small. Finally, the YF model with the elevated *Vp*/*Vs* ratio (1.9 versus ~1.8 in IASP91) in the depth interval from 85 to 200 km and the standard ratio elsewhere yields the observed residuals (around −2 s). To conclude, the early arrivals of *S*410*p* can be caused by the anomalously high *Vp*/*Vs* ratio.

[17] An alternative reason for the early arrivals of *S*410*p* is the topography of the 410 km discontinuity. The travel-time effect dT of the perturbation of the interface depth dH is [*Farra & Madariaga*, 1988]

$$dT = (pz1 - pz2)dH,$$

where $pz1$ and $pz2$ are the vertical slownesses of the incident and transmitted wave, respectively. For the slowness of 10.5 s/°, the perturbation of the *Sp* travel time is −0.12 dH and that of the *S* travel-time is 0.01 dH. Therefore the perturbation of the *Sp* travel time relative to the *S* travel time is −0.13 dH. For $dH = 15$ km, the perturbation of time is −1.95 s. In other words, the residuals of ~−2 s can be explained by a depression of ~15 km on the 410 km discontinuity.

4. Observations of *S*350*p* and *S*480*p*

[18] Seismic phases recorded in the vicinity of *S*410*p* are another target of our analysis. We employed two methods of analysis. In the first method we investigate the waveforms of *S*410*p* at each station and in each azimuthal sector. The stacked *SV* component of the receiver function consists of the main lobe and two sidelobes with opposite polarity. The amplitude ratio between the sidelobes and the main lobe is close to 0.4. The *Sp* phase from a boundary between two half-spaces should have practically the same form as the parent *SV* phase, except for the polarity.

[19] We inspected the amplitude ratio between the positive right-hand sidelobe of the *S*410*p* phase and its main

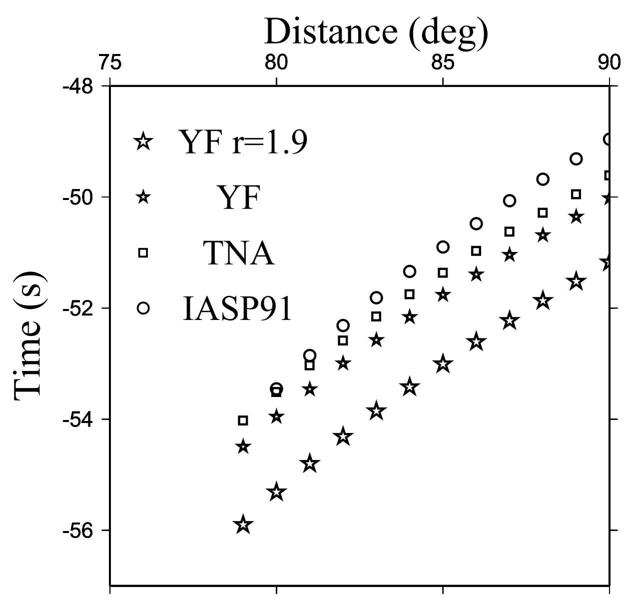

Figure 9. Arrival times of *S*410*p* as functions of epicentral distance for IASP91 (circles), *S* velocity profile for TNA and *Vp*/*Vs* ratio of IASP91 (squares), *S* velocity profile for YF and the *Vp*/*Vs* ratio of IASP91 (small stars), and *S* velocity profile and the *Vp*/*Vs* ratio = 1.9 in the interval between 85 and 200 km of IASP91 outside this interval (large stars).

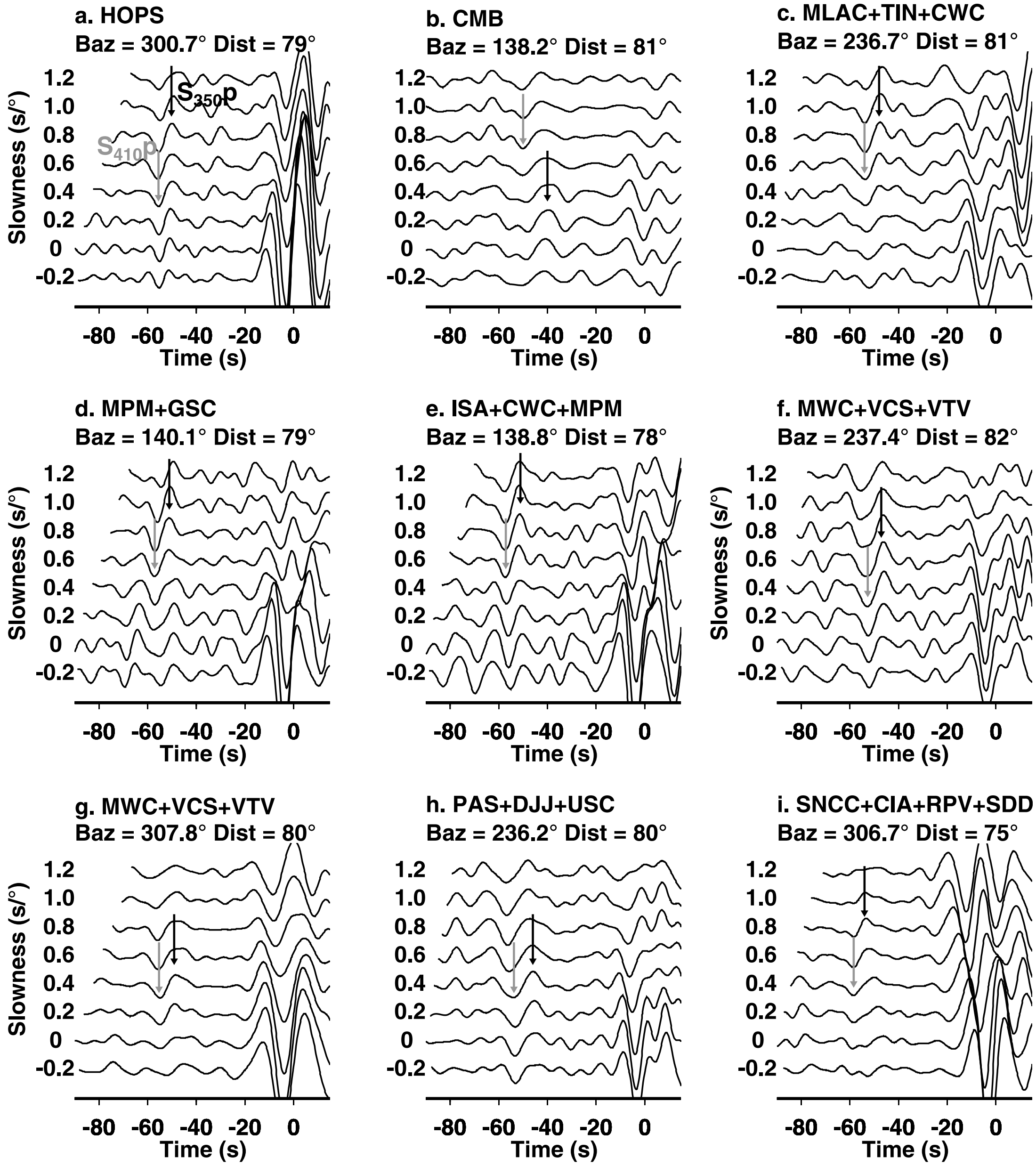

Figure 10. Examples of the *P* components of SRFs with arrivals of *S*350*p*. Arrivals of *S*410*p* and *S*350*p* are marked by arrows at the traces with the largest amplitudes.

lobe for those receiver functions, where the *S*410*p* amplitude exceeds the threshold of 3σ (see section 3), and the maximum of each amplitude is observed within the slowness range from 0 to 1.2 s/°. The largest amplitude in this slowness range is taken for the amplitude estimate. The results are presented in the histogram in Figure 6b and in Table 1.

[20] The histogram in Figure 6b is bimodal, with one maximum between 0.4 and 0.5 and the second maximum between 0.7 and 0.9. Examples of the receiver functions contributing to the first and second maxima are shown in Figures 4 and 10, respectively. We interpret the histogram maximum between 0.4 and 0.5 as mainly an effect of the sidelobe of *S*410*p*. In Table 1 we marked the receiver functions that contribute to the maximum between 0.7 and 0.9; the others either contribute to the first maximum or, sometimes, are too complicated for accurate measurements. Random noise cannot be the reason for the second maximum because the elevated amplitude ratio is observed systematically in three azimuths at the large group of stations. On a global scale this phenomenon is rare, only in about 10% of the data [*Vinnik and Farra*, 2007], and mostly in a specific group of continental regions. A difference in attenuation between the *S* and *S*410*p* phases was tested as a possible explanation for the anomalously large amplitude of the sidelobe, with a negative result [*Vinnik and Farra*, 2007]. Moreover, there are examples of a large signal that arrives at the time appropriate for the sidelobe in the absence of the main lobe (see example in Figure 11h). The only plausible explanation for the second maximum that we can

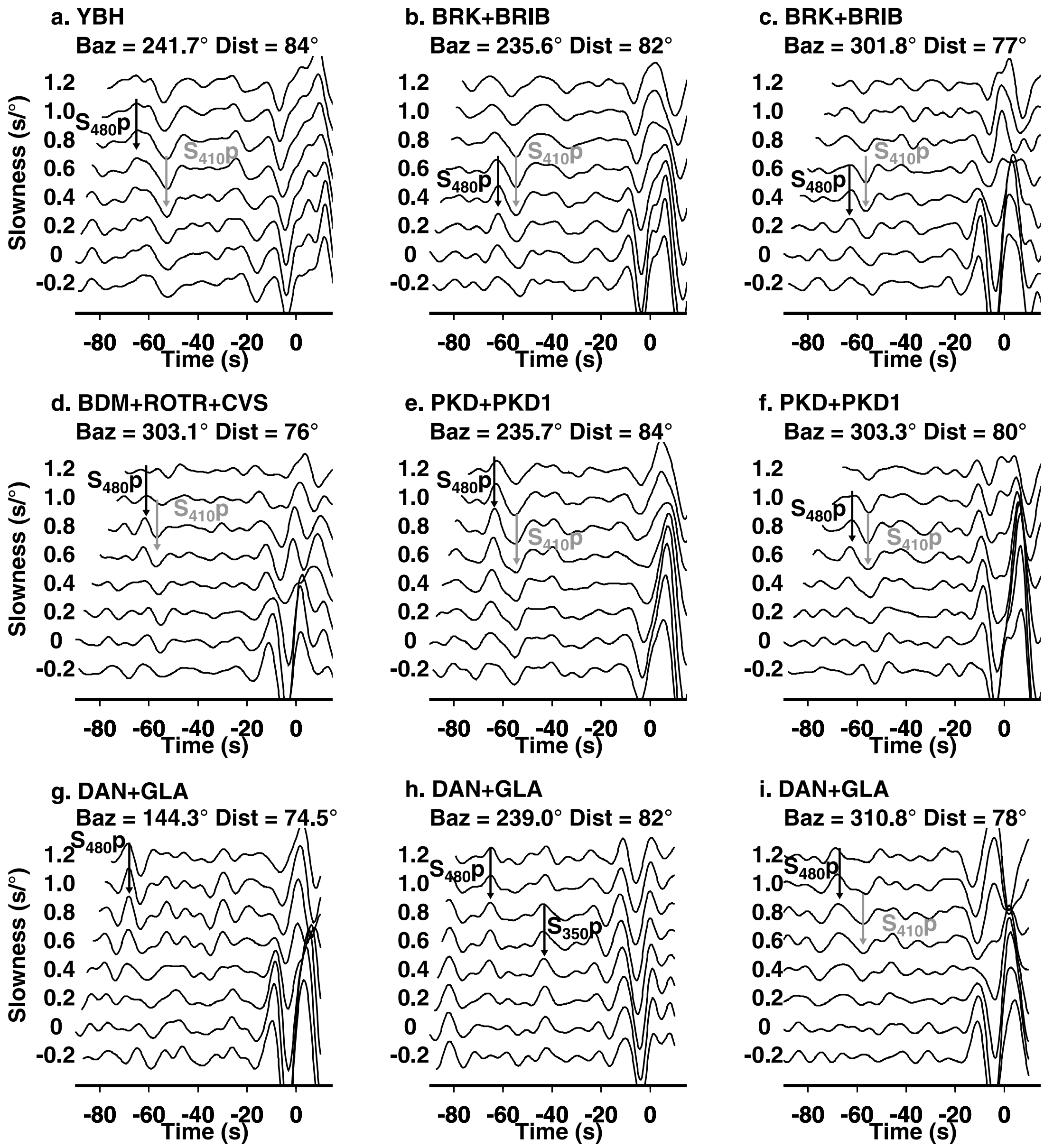

Figure 11. The same as Figure 10, but for *S*480*p*.

suggest is the systematic presence of another phase interfering constructively with the sidelobe. This can be the *Sp* phase from the negative 350 km discontinuity, which in several other regions presents the upper bound of a thin low *S* velocity layer atop the 410 km discontinuity [*Vinnik and Farra,* 2002, 2007].

[21] The stations in Table 1 are sorted by latitude from north to south. It is easy to see that the large amplitude ratio is found at almost all southern stations, whereas at the northern stations such ratio is rare. Approximate geographical locations of the 350 km discontinuity corresponding to the data in Table 1 with a large ratio between the right-side lobe and the main lobe of *S*410*p* are also shown in Figure 12, and they display the same trend.

[22] Our interpretation is verified by synthetic seismograms (Figure 13). The synthetics were calculated with the reflectivity techniques [*Fuchs and Mueller*, 1971] for the standard IASP91 model and a modified IASP91 model with a low-velocity layer atop the 410 km discontinuity. The *S* velocity in the middle of the layer is 2.5% lower than in the standard model, and the *Vp*/*Vs* ratio is that of the IASP91 model. The synthetics were processed like the actual seismograms, and the receiver functions were stacked in the distance range from 75° to 85°. In the synthetic SRFs for the modified model the right-hand side lobe of *S*410*p* is comparable in amplitude with *S*410*p*, as in the examples in Figure 10. This model is not unique, but the approximate depth of the low-velocity layer and the *S* velocity reduction are constrained by the time and amplitude of the related *S*350*p* phase. The label "*S*350*p*" for this phase does not imply that the 350 km discontinuity is sharp and located precisely at a depth of 350 km, but it is within the range from 320 to 380 km.

[23] Another exotic arrival, *S*480*p* (Figure 11), has the same positive polarity as *S*350*p*, which implies a negative

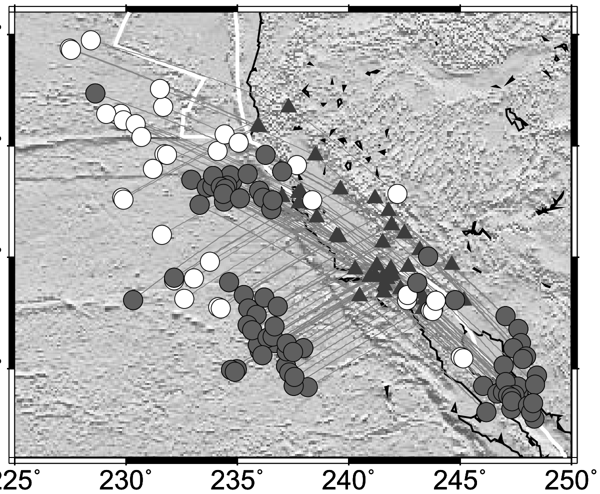

Figure 12. Locations of the 350 km discontinuity attributed to the surface projections of the piercing points of *S*410*p* (gray circles). These data correspond to the large (not less than 0.7) amplitude ratio between the right-hand sidelobe and the main lobe of *S*410*p* in Table 1. The data corresponding to a small amplitude ratio are shown by white circles. The seismograph stations are shown by black triangles.

(with a lower *S* velocity at the lower side) 480 km discontinuity. As in the case of the 350 km discontinuity, the term "480 km" does not mean that the discontinuity is sharp and its depth is precisely 480 km. *S*480*p* may interfere constructively with the left-hand side lobe of *S*410*p*, and Figure 11 demonstrates examples of the arrivals, where the signal is large relative to the RMS value of noise, comparable in amplitude with *S*410*p*, and is observed in the differential slowness range appropriate for a conversion depth of 480 km. Two examples (Figures 11g and 11h) are remarkable in the fact that *S*410*p* is missing, and *S*480*p* cannot be interpreted as a sidelobe of *S*410*p*. Some receiver functions demonstrate complicated wavefields, which suggest that the 480 km discontinuity may present part of a still unresolved structure in the transition zone.

[24] Another way of representing receiver functions is common conversion point stacking [*Dueker and Sheehan*, 1997], implemented for the *S* receiver functions by *Wittlinger et al.* [2004]. In this method Earth's medium is divided into boxes 100 km × 1000 km × 5 km, where 100 and 1000 km correspond to the horizontal directions parallel and perpendicular to the azimuth of 135° (purple line in Figure 7), respectively, and 5 km is for the vertical direction. *P* component amplitudes of the SRFs are weighted as described in section 2 and summed for the *Sp* rays with the conversion points within the box. The sum is attributed to the center of the box. The number of rays in most of the boxes is more than 90. Migration is performed by using the YF model with the elevated *Vp*/*Vs* ratio between 85 and 220 km depths. The obtained image (Figure 14) demonstrates the arrivals from the 410 and 350 km discontinuities with comparable amplitudes. In agreement with the data in Table 1 and Figure 12, the largest amplitudes of *S*350*p* are in the south of the section, while the signal practically disappears in the north. No systematic pattern is found for *S*480*p*.

5. Discussion and Conclusions

[25] We have found that in most cases the arrivals of *S*410*p* are early, about 2 s earlier than in the standard IASP91 model. The early arrivals may have two reasons: anomalously high *Vp*/*Vs* ratio and a depressed 410 km discontinuity. There are independent indications that elevated *Vp*/*Vs* ratio may occur in the study region. Temperature variations in the mantle lead to variations of seismic velocities and of the related teleseismic travel-time residuals relative to the 1-D model. The expected slope of the regression line between the teleseismic *S* and *P* residuals for the standard *Vp*/*Vs* ratio is 2.7 [*Vinnik et al.*, 1999]. However, the slope determined from the residuals at seismograph stations in North America is around 3.6 or more [*Hales and Roberts*, 1970; *Wickens and Buchbinder*, 1980; *Romanowicz and Cara*, 1980; *Vinnik et al.*, 1999]. Velocities in active tectonic regions in the west of North America are lower than in the cratonic regions in the east, and the elevated slope of the regression line implies either a reduced *Vp*/*Vs* ratio in the east, an elevated *Vp*/*Vs* ratio in the west, or both. The elevated *Vp*/*Vs* ratio is usually attributed to high anelastic attenuation and the related relaxation of shear modulus. Melting can be responsible for a very high *Vp*/*Vs* ratio [*Hammond and Humphreys*, 2000].

[26] The issue of the depth of the 410 km discontinuity beneath California is controversial. At two stations in California the time difference between *P*660*s* and *P*410*s* is reduced by ~0.6 s relative to IASP91 [*Vinnik et al.*, 1999]. This effect can be caused by a depression of ~5 km on the 410 km discontinuity. A reduced by ~30 km thickness of the mantle transition zone was inferred from the *P* receiver functions of station PAS in California [*Gurrola and Minster*, 1998], but this estimate is questionable [*Chevrot et al.*, 1999]. In the *P* receiver functions from a few stations in California there is no systematic deviation of the time difference between *P*660*s* and *P*410*s* from the standard value [*Ramesh et al.*, 2002]. A reduction of thickness of the mantle transition zone beneath the Pacific and North

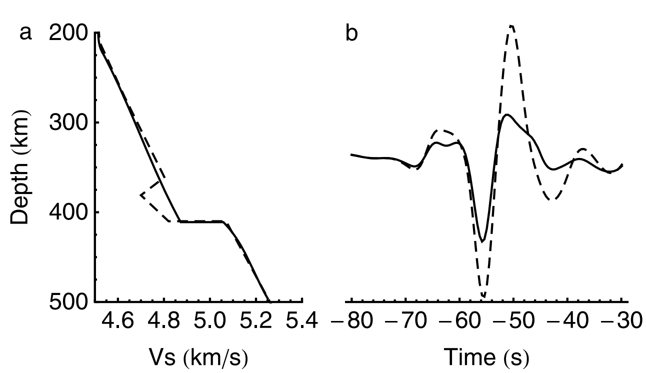

Figure 13. (a) *S* velocity profiles and (b) the related *P* components of synthetic SRFs. Solid and dashed lines are for IASP91 model and the modified model with a low velocity atop the 410 km discontinuity, respectively.

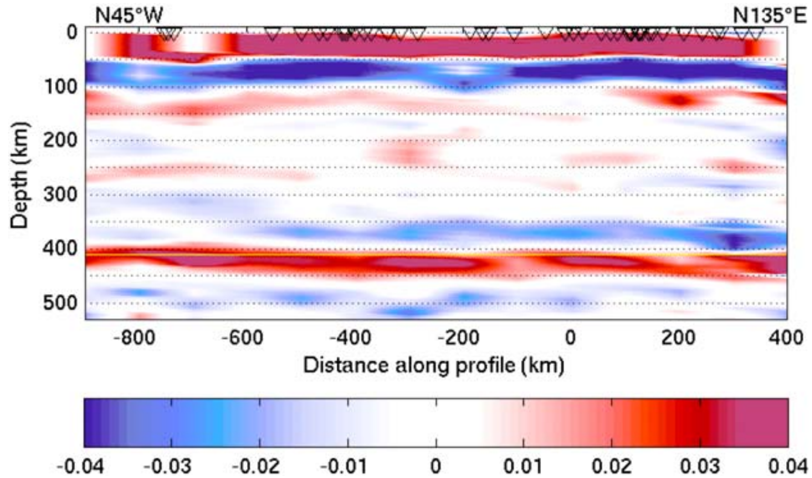

Figure 14. Common conversion point CCP stack of the SRFs. Location of the section plane is shown in Figure 7 (purple line). The distance axis has its origin at 35.5°N, 118.5°W; the positive direction is in the azimuth of 135°. The migrated amplitudes are represented by color code, with blue (respectively red) corresponding to negative (respectively positive) impedance contrast. For migration we use the *S* wave velocity model of *Yang and Forsyth* [2006]. The *Vp*/*Vs* ratio between 85 and 200 km depths is 1.9; outside this depth interval the ratio is equal to that in IASP91 [*Kennett and Engdahl*, 1991].

America was inferred by *Flanagan and Shearer* [1998] and *Gu et al.* [1998] from observations of precursors to *SS*. This discontinuity corresponds mainly to the phase transition from olivine to wadsleyite with a positive Clapeyron slope of about 3 MPa/K [*Katsura and Ito*, 1989], and a depression of ~10 km requires a temperature elevated by ~100°.

[27] Our observations of the *S*350*p* phase suggest the presence of a thin (a few tens of kilometers wide) low *S* velocity layer atop the 410 km discontinuity beneath both California and the neighboring margin of the Pacific. Observations of this phase outside California with the same technique are rare: the analysis of *S* receiver functions of more than 50 globally distributed stations revealed this phase at several locations: the Kaapvaal craton and Siberian craton [*Vinnik and Farra*, 2002], the Arabian plate, western Siberia, north China, south China, West Africa, and Antarctica [*Vinnik and Farra*, 2007]. Earlier, the anomalies beneath north China and Kaapvaal craton were inferred from the analysis of multiple *ScS* reverberations [*Revenaugh and Sipkin*, 1994] and *P* receiver functions [*Vinnik et al.*, 1996], respectively. Most of these regions are large igneous provinces (LIPs) of Mesozoic and Cenozoic age within Precambrian platforms. The same layer was found at three locations in the west of North America [*Song et al.*, 2004; *Gao et al.*, 2006; *Jasbinsek and Dueker*, 2007].

[28] The low *S* velocity atop the 410 km discontinuity can be related to a high solubility of water in wadsleyite in the mantle transition zone relative to olivine in the overlying mantle: up to about 2 wt % below the 410 km discontinuity versus 0.2 wt % over it [e.g., *Bolfan-Casanova*, 2005]. Then, if the water content in the transition zone is higher than the solubility atop the 410 km discontinuity, mantle upwelling across the 410 km discontinuity leads to dehydration and melting on the upper side of the discontinuity [e.g., *Kawamoto et al.*, 1996; *Bercovici and Karato*, 2003]. The reduction of *S* velocity by 2%, which is consistent with our data, requires ~1% melt porosity [*Kreutzmann et al.*, 2004].

[29] The origin of the low velocity atop the 410 km discontinuity was attributed either to dehydration of subducted lithospheric plates [*Revenaugh and Sipkin*, 1994; *Song et al.*, 2004; *Jasbinsek and Dueker*, 2007] or mantle plumes [*Vinnik and Farra*, 2002, 2007]. Our present observations favor the second hypothesis: a well-known hot spot (Baja Guadalupe, 27°N, 113°W) is located in the south of the study region (Figure 7), and the largest *S*350*p* phases are observed at the southernmost stations, in the vicinity of this hot spot. Of course water could be originally brought to the mantle in subduction zones and later transported by a plume to the 410 km discontinuity. In the northwestern United States the low-velocity layer [*Song et al.*, 2004] can be associated with the Columbia River flood basalts and the related mantle plume [*Vinnik and Farra*, 2007]. The low velocity atop the 410 km discontinuity can alternatively be caused by carbonate with a low melting temperature [*Presnall and Gudfinnsson*, 2005].

[30] Observations of the *S*480*p* phase in California which are indicative of a low *S* velocity layer in the transition zone were previously made with the same technique in several other regions, some of them related to hot spots and Mesozoic-Cenozoic LIPs: Iceland [*Vinnik et al.*, 2005], Afar, Ethiopia [*Vinnik et al.*, 2004], Cameroon and north China [*Vinnik and Farra*, 2006], and southern Africa [*Vinnik et al.* 2009]. A clear recording of *S*480*p* with the piercing point beneath the Baja Guadalupe hot spot has been obtained at station TUC in the west of the United States [*Vinnik and Farra*, 2006]. This layer beneath California and the Pacific margin can be related to the neighboring large-scale, low-velocity anomaly in the transition zone [*Ritsema et al.*, 2004]. The origin of this layer requires further research, but its possible association with hot spots and low-velocity anomalies in the transition zone suggests a relation to elevated temperature.

[31] **Acknowledgments.** The seismograms were obtained from the Berkeley Digital Seismic Network, the Southern California network, and IRIS DMC. L.V. and S.K. are partly supported by grant 07-05-00315 from the Russian Fund for Basic Research. S.K. was partly supported by the collaboration program between the Institut de Physique du Globe de Paris and the Institute of Physics of the Earth of the RAS, Moscow. The authors appreciate constructive comments from the section editor and two anonymous reviewers. This is IPGP contribution 2646.

References

Atwater, T. (1989), Plate tectonic history of the northeast Pacific and western North America, in *The Geology of North America*, vol. N, *The Eastern Pacific Ocean and Hawaii*, edited by E. L. Winterer, D. M. Hussong, and R. W. Decker, pp. 21–72, Geol. Soc. of Am., Boulder, Colo.

Benz, H. M., G. Zandt, and D. H. Oppenheimer (1992), Lithospheric structure of Northern California from teleseismic images of the upper mantle, *J. Geophys. Res.*, *97*(B4), 4791–4807.

Bercovici, D., and S.-I. Karato (2003), Whole-mantle convection and the transition-zone filter, *Nature*, *425*, 39–44, doi:10.1038/nature01918.

Bolfan-Casanova, N. (2005), Water in the Earth's mantle, *Mineral. Mag.*, *69*(3), 229–257, doi:10.1180/0026461056930248.

Chevrot, S., L. Vinnik, and J.-P. Montagner (1999), Global-scale analysis of the mantle *Pds* phases, *J. Geophys. Res.*, *104*, 20,203–20,219, doi:10.1029/1999JB900087.

Dueker, K. G., and A. F. Sheehan (1997), Mantle discontinuity structure from mid-point stacks of converted *P* to *S* waves across the Yellowstone hotspot track, *J. Geophys. Res.*, *102*, 8313–8327, doi:10.1029/96JB03857.

Farra, V., and R. Madariaga (1988), Non-linear reflection tomography, *Geophys. J.*, *95*, 135–147, doi:10.1111/j.1365-246X.1988.tb00456.x.

Farra, V., and L. Vinnik (2000), Upper mantle stratification by *P* and *S* receiver functions, *Geophys. J. Int.*, *141*, 699–712, doi:10.1046/j.1365-246x.2000.00118.x.

Flanagan, M. P., and P. M. Shearer (1998), Global mapping of topography on transition zone velocity discontinuity by stacking *SS* precursors, *J. Geophys. Res.*, *103*, 2673–2692, doi:10.1029/97JB03212.

Fuchs, K., and G. Mueller (1971), Computation of synthetic seismograms with reflectivity method and comparison with observations, *Geophys. J. R. Astron. Soc.*, *23*, 417–433.

Gao, W., E. Matzel, and S. P. Grand (2006), Upper mantle seismic structure beneath eastern Mexico determined from *P* and *S* waveform inversion and its implications, *J. Geophys. Res.*, *111*, B08307, doi:10.1029/2006JB004304.

Grand, S. P., and D. V. Helmberger (1984), Upper mantle shear structure of North America, *Geophys. J. R. Soc. Lond.*, *76*, 399–438.

Gu, Y. J., A. M. Dziewonski, and C. B. Agee (1998), Global de-correlation of the topography of the transition zone discontinuities, *Earth Planet. Sci. Lett.*, *157*, 57–67, doi:10.1016/S0012-821X(98)00027-2.

Gurrola, H., and J. B. Minster (1998), Thickness estimates of the upper-mantle transition zone from bootstrapped velocity spectrum stacks of receiver functions, *Geophys. J. Int.*, *133*, 31–43, doi:10.1046/j.1365-246X.1998.1331470.x.

Hales, A. L., and J. L. Roberts (1970), The travel times of *S* and *SKS*, *Bull. Seismol. Soc. Am.*, *57*, 461–489.

Hammond, W. C., and E. D. Humphreys (2000), Upper mantle seismic wave velocity: Effects of realistic partial melt geometries, *J. Geophys. Res.*, *105*, 10,975–10,986, doi:10.1029/2000JB900041.

Jasbinsek, J., and K. Dueker (2007), Ubiquitous low-velocity layer atop the 410-km discontinuity in the northern Rocky Mountains, *Geochem. Geophys. Geosyst.*, *8*, Q10004, doi:10.1029/2007GC001661.

Katsura, T., and E. Ito (1989), The system Mg_2SiO_4-Fe_2SiO_4 at high pressures and temperatures: Precise determination of stabilities of olivine, modified spinel, and spinel, *J. Geophys. Res.*, *94*, 15,663–15,670, doi:10.1029/JB094iB11p15663.

Kawamoto, T., R. Hervig, and J. Holloway (1996), Experimental evidence for a hydrous transition zone in the early Earth's mantle, *Earth Planet. Sci. Lett.*, *142*, 587–592, doi:10.1016/0012-821X(96)00113-6.

Kennett, B. L. N., and E. R. Engdahl (1991), Travel times for global earthquake location and phase identification, *Geophys. J. Int.*, *105*, 429–465, doi:10.1111/j.1365-246X.1991.tb06724.x.

Kreutzmann, A., G. Marquart, I. T. Bjarnson, H. Schmeling, A. Junge, and T. Ruedas (2004), Temperature and melting of a ridge-centered plume with application to Iceland: Part II. Predictions for electromagnetic and seismic observables, *Geophys. J. Int.*, *159*, 1097–1111, doi:10.1111/j.1365-246X.2004.02397.x.

Melbourne, T., and D. Helmberger (2001), Mantle control of plate boundary deformation, *Geophys. Res. Lett.*, *28*, 4003–4006, doi:10.1029/2001GL013167.

Presnall, D. C., and G. H. Gudfinnsson (2005), Carbonate-rich melts in the oceanic low-velocity zone and deep mantle, in *Plates, Plumes and Paradigms*, edited by G. R. Foulger, J. H. Natland, D. C. Presnall, and D. L. Anderson, pp. 207–216, Geol. Soc. of Am., Boulder, Colo.

Ramesh, D. S., R. Kind, and X. Yuan (2002), Receiver function analysis of the North American crust and upper mantle, *Geophys. J. Int.*, *150*, 91–108, doi:10.1046/j.1365-246X.2002.01697.x.

Revenaugh, J., and S. Sipkin (1994), Seismic evidence for silicate melt atop the 410-km discontinuity, *Nature*, *369*, 474–476, doi:10.1038/369474a0.

Ritsema, J., H. J. van Heijst, and J. H. Woodhouse (2004), Global transition zone tomography, *J. Geophys. Res.*, *109*, B02302, doi:10.1029/2003JB002610.

Romanowicz, B., and M. Cara (1980), Reconsideration of the relations between *S* and *P* station anomalies in North America, *Geophys. Res. Lett.*, *7*, 417–420, doi:10.1029/GL007i006p00417.

Simmons, N. A., and H. Gurrola (2000), Multiple seismic discontinuities near the base of the transition zone in the Earth's mantle, *Nature*, *405*, 559–562, doi:10.1038/35014589.

Song, T. A., D. W. Helmberger, and S. P. Grand (2004), Low-velocity zone atop the 410-km seismic discontinuity in the northwestern United States, *Nature*, *427*, 530–533, doi:10.1038/nature02231.

Tanimoto, N., and K. P. Sheldrake (2002), Three-dimensional *S*-wave velocity structure in southern California, *Geophys. Res. Lett.*, *29*(8), 1223, doi:10.1029/2001GL013486.

Thurber, C., H. Zhang, T. Brocher, and V. Langeheim (2009), Regional three-dimensional seismic velocity model of the crust and uppermost mantle of northern California, *J. Geophys. Res.*, *114*, B01304, doi:10.1029/2008JB005766.

Vinnik, L. P., and V. Farra (2002), Subcratonic low-velocity layer and flood basalts, *Geophys. Res. Lett.*, *29*(4), 1049, doi:10.1029/2001GL014064.

Vinnik, L. P., and V. Farra (2006), *S* velocity reversal in the mantle transition zone, *Geophys. Res. Lett.*, *33*, L18316, doi:10.1029/2006GL027120.

Vinnik, L., and V. Farra (2007), Low *S* velocity atop the 410-km discontinuity and mantle plumes, *Earth Planet. Sci. Lett.*, *262*, 398–412, doi:10.1016/j.epsl.2007.07.051.

Vinnik, L. P., R. W. E. Green, L. O. Nicolaysen, G. L. Kosarev, and N. V. Petersen (1996), Deep structure of the Kaapvaal craton, *Tectonophysics*, *262*, 67–75, doi:10.1016/0040-1951(96)00012-1.

Vinnik, L., S. Chevrot, J.-P. Montagner, and F. Guyot (1999), Teleseismic travel time residuals in North America and anelasticity of the asthenosphere, *Phys. Earth Planet. Inter.*, *116*, 93–103, doi:10.1016/S0031-9201(99)00132-6.

Vinnik, L. P., V. Farra, and R. Kind (2004), Deep structure of the Afro-Arabian hotspot by S receiver functions, *Geophys. Res. Lett.*, *31*, L11608, doi:10.1029/2004GL019574.

Vinnik, L. P., G. R. Foulger, and Z. Du (2005), Seismic boundaries in the mantle beneath Iceland: A new constraint on temperature, *Geophys. J. Int.*, *160*, 533–538, doi:10.1111/j.1365-246X.2005.02529.x.

Vinnik, L. P., S. Oreshin, G. Kosarev, S. Kiselev, and L. Makeyeva (2009), Mantle anomalies beneath southern Africa: Evidence from seismic *S* and *P* receiver functions, *Geophys. J. Int.*, *179*, 279–298, doi:10.1111/j.1365-246X.2009.04261.x.

Wickens, A. J., and G. G. R. Buchbinder (1980), *S*-wave residuals in Canada, *Bull. Seismol. Soc. Am.*, *70*, 809–822.

Wittlinger, G., V. Farra, and J. Vergne (2004), Lithospheric and upper mantle stratifications beneath Tibet: New insights from *Sp* conversions, *Geophys. Res. Lett.*, *31*, L19615, doi:10.1029/2004GL020955.

Yang, Y., and D. W. Forsyth (2006), Rayleigh wave phase velocities, small-scale convection, and azimuthal anisotropy beneath southern California, *J. Geophys. Res.*, *111*, B07306, doi:10.1029/2005JB004180.

Yang, Y., M. H. Ritzwoller, F.-C. Lin, M. P. Moschetti, and N. M. Shapiro (2008), Structure of the crust and uppermost mantle beneath the western United States revealed by ambient noise and earthquake tomography, *J. Geophys. Res.*, *113*, B12310, doi:10.1029/2008JB005833.

Zandt, G., H. Gilbert, T. J. Owens, M. Ducea, J. Saleeby, and C. H. Jones (2004), Active foundering of a continental arc root beneath the southern Sierra Nevada in California, *Nature*, *431*, 41–46, doi:10.1038/nature02847.

V. Farra, Y. Ren, and E. Stutzmann, Institut de Physique du Globe de Paris, 75005 Paris, France. (stutz@ipgp.jussieu.fr)

S. Kiselev and L. Vinnik, Institute of Physics of the Earth, 123995 Moscow, Russia. (vinnik@ifz.ru)